Dual-mode imaging with radiolabeled gold nanorods

Ashish Agarwal
Xia Shao
Justin R. Rajian
Huanan Zhang
David L. Chamberland
Nicholas A. Kotov
Xueding Wang

Dual-mode imaging with radiolabeled gold nanorods

Ashish Agarwal,[a] **Xia Shao,**[b] **Justin R. Rajian,**[b] **Huanan Zhang,**[a] **David L. Chamberland,**[c] **Nicholas A. Kotov,**[a]
and Xueding Wang[b]
[a]University of Michigan, Department of Chemical Engineering, Ann Arbor, Michigan 48109
[b]University of Michigan, Department of Radiology, Ann Arbor, Michigan 48109
[c]Rheumatology Associates, Medford, Oregon 97504

Abstract. Many nanoparticle contrast agents have difficulties with deep tissue and near-bone imaging due to limited penetration of visible photons in the body and mineralized tissues. We are looking into the possibility of mediating this problem while retaining the capabilities of the high spatial resolution associated with optical imaging. As such, the potential combination of emerging photoacoustic imaging and nuclear imaging in monitoring of antirheumatic drug delivery by using a newly developed dual-modality contrast agent is investigated. The contrast agent is composed of gold nanorods (GNRs) conjugated to the tumor necrosis factor (TNF-α) antibody and is subsequently radiolabeled by ^{125}I. ELISA experiments designed to test TNF-α binding are performed to prove the specificity and biological activity of the radiolabeled conjugated contrast agent. Photoacoustic and nuclear imaging are performed to visualize the distribution of GNRs in articular tissues of the rat tail joints *in situ*. Findings from the two imaging modalities correspond well with each other in all experiments. Our system can image GNRs down to a concentration of 10 pM in biological tissues and with a radioactive label of 5 μCi. This study demonstrates the potential of combining photoacoustic and nuclear imaging modalities through one targeted contrast agent for noninvasive monitoring of drug delivery as well as deep and mineralized tissue imaging.
© *2011 Society of Photo-Optical Instrumentation Engineers (SPIE)*. [DOI: 10.1117/1.3580277]

Keywords: dual-mode imaging; targeted contrast agents; photoacoustic tomography; nuclear imaging; gold nanoparticles.

Paper 10583SSRRR received Oct. 27, 2010; revised manuscript received Mar. 28, 2011; accepted for publication Mar. 28, 2011; published online May 12, 2011.

1 Introduction

Nanoparticle bioconjugates represent contrast agents for a variety of imaging and treatment techniques that take advantage of unique light-absorption, emissive, or magnetic properties of quantum-confined solids.[1–5] One of them, photoacoustic imaging (PAI), is a nonionizing, noninvasive biomedical imaging modality that combines the merits of both light and ultrasound.[6–9] In PAI, a short-pulsed laser is used to illuminate the tissue and generate photoacoustic waves due to thermoelastic expansion. The laser-generated signal is then measured by broadband ultrasound transducers to reconstruct the image in the tissue sample. PAI is highly sensitive to the optical absorption contrast in the tissue, while its spatial resolution is limited mainly by ultrasound detection rather than by the overwhelming light scattering as in diffuse optical imaging.

The application of PAI holds promise for evaluation at the molecular or cellular level due to the high sensitivity of PAI to a variety of extrinsic optical contrast agents. Several organic dyes and metallic nanoparticles (NPs) have been studied as PAI contrast agents in the past decade. Wang et al. have demonstrated enhanced photoacoustic signal from indocyanine green (ICG), an FDA approved dye that absorbs light in the near-infrared region.[10] Copland et al. have developed ICG embedded ormosil particles conjugated with HER2 for targeted imaging of breast cancer cells.[11] More recently Song et al. have used methyline blue as a contrast agent to detect sentinel lymph node.[12] In com-

parison to the contrast agents based on organic dyes, metallic NPs could have better stability, less photobleaching and greater flexibility of tuning their optical spectra, although further investigation is necessary to reduce their toxicity before large-scale clinical use can occur.[13] Most of the metallic NP contrast agents explored for the enhancement of PAI sensitivity are based on gold, which is a biocompatible material. Yang et al. studied gold nanocages to evaluate the cerebral vortex in rats.[14] Wang et al. used gold nanoshells for studying rat brain.[15] Contrast agent-based gold nanorods (GNRs) have been developed and studied extensively by our group for tumor targeting/imaging and monitoring antirheumatic drug delivery.[16–18] Other than performing as contrast agents for imaging, gold NPs have also been widely used as vehicles to achieve drug delivery and agents for photothermal therapeutics.[19–21]

Despite the variety and relative effectiveness of PAI contrast agents available, there is an inherent disadvantage in PAI measurements due to the strong attenuation of light in biological tissues as well as the high background signal as a result of intrinsic tissue optical absorption. PAI presents local spatial resolution on the submillimeter level; however, the penetration depth limits its ability to make measurements with a satisfactory signal-to-noise ratio deep inside the tissue. In fact, the same problem is present for all NP contrast agents based on optical emission, which has become popular recently.[22,23] This inherent problem of light emission can be overcome indirectly by merging it with another imaging modality that can provide a high signal-to-noise ratio even deep inside the tissue and assist to validate the findings of the other technique.

Address all correspondence to: Xueding Wang, University of Michigan, Department of Radiology, 1301 Catherine Streeet, 3226B Med Sci 1, Ann Arbor, Michigan 48109-5667. Tel: 734-647-2728; Fax: 734-764-8541; E-mail: xdwang@umich.edu

In this study, we have successfully fabricated a targeted optical and nuclear dual-modality agent by radiolabeling GNRs with [^{125}I] for potential *in vivo* monitoring of anti-tumor necrosis factor (TNF-α) drug delivery. The high contrast-to-noise ratio and good quantification of nuclear imaging provide a gold standard and assist to validate PAI findings, while PAI helps overcome the spatial resolution limitations of nuclear imaging and demonstrates regional information with improved accuracy. As demonstrated in our initial experiments on rat joints *in situ*, the distribution of radiolabeled GNRs in articular tissue can be presented by both PAI and single-photon emission computed tomography (SPECT). Moreover, by covalent binding of radioisotopes on the surface of targeted gold NPs, nuclear imaging, such as positron emission tomography (PET) and SPECT, can for the first time image the concentration and distribution of gold NP-based agents *in vivo*, which could contribute considerably to understanding of the toxicity and pharmacokinetics of any novel gold nanocolloids in the future.

2 Materials and Methods

2.1 *PAI Setup*

The photoacoustic experimental setup is given in Fig. 1. Laser pulses from an optical parametric oscillator (Vibrant B, Opotek) pumped by an Nd:YAG laser (Brilliant B, Bigsky) were used to illuminate the sample, either an ELISA well plate, as in Fig. 1(a), or joints in a rat tail, as in Fig. 1(b). The laser pulse repetition rate was 10 Hz, and each pulse had a width of 5.5 ns. The laser wavelength was tuned to 760 nm, the absorption peak of the GNRs. An optical diffuser was used to expand the laser beam to cover a well or a joint completely. The energy density of the laser pulses incident at the sample was adjusted to <10 mJ/cm^2, within the ANSI safety limit. Part of the laser beam was reflected off by a glass plate and measured by using a photodiode in order to take into account the incident light energy and the laser fluctuation. Neutral density filters were placed in the beam path to limit the maximum amount of light entering into the photodiode.

For the experiment on the ELISA well plate, an unfocused ultrasonic transducer (XMS-310, Panametrics, Waltham, Massachusetts) with a central frequency of 10 MHz, –6 dB-bandwidth of 133% and a diameter of 2 mm was used to collect the photoacoustic signals from the illuminated well. Part of the well and the transducer were immersed in water for acoustic coupling. For the imaging of rat tail joints, a focused transducer (V312, Panametrics) with a central frequency of 10 MHz, –6-dB bandwidth of 130%, a diameter of 0.25 in., and a focal length of 0.75 in. was used to conduct a raster scan along the length of

the tail. The –3-dB focal diameter of this transducer is 0.47 mm. Photoacoustic signals received by the transducer were amplified (PR5072, Panametrics) and sent into one channel of a digital oscilloscope (TDS 540B, Tektronics), which was triggered by the laser firing. The signal from the photodiode was sent into another channel of the oscilloscope. The signals received by the oscilloscope were digitized, collected, and stored in a computer for processing and analysis. The amplitude of the photoacoustic signal was divided by the photodiode signal amplitude to get the photoacoustic response.

2.2 *γ Imaging Setup*

Radionuclide imaging was performed using the Gamma Imager (Biospace Lab, Paris). The planar imaging for ELISA experiments was performed with the Gamma Imager detection area facing upward, an ELISA well plate was placed directly on the parallel-hole collimator 1.3/0.2/20 (hole diameter/septum thickness/height in millimeters). Fifteen-minute duration image was acquired using an energy window of 15–70 KeV, and the image was then displayed and quantified using Gamma Vision + software (Version 3.0). Radioactivity was determined by drawing regions of interest and calculated based on a standard curve, which is generated by scanning a series of standards with known radioactivities.

2.3 *Micro–Single-Photon Emission Computed Tomography/Computed Tomography*

SPECT/computed tomography (CT) was performed using a pair of collimators (1.3/0.2/35) that stand up to orient the detection area toward the animal (rat tail). The rat tail was fixed on a holder and aligned parallel to the face of detector. After a 36-min CT scan, a 30-min γ imaging was acquired and 2-D image was reconstructed using γ acquisition software. The reconstructed fusion image of SPECT/CT could be displayed and quantified using Amira software (Version 3.1).

2.4 *Synthesis of Gold Nanorods*

GNRs are synthesized by a method modified from literature.[24–27] Briefly, a seed solution is prepared by reducing Gold (III) Chloride (25 μL, 0.05 M) in hexadecyltrimethyl ammonium bromide (4.7 ml, 0.1 M) by addition of freshly prepared sodium borohydride (0.3 ml, 0.01 M) under vigorous stirring. An aliquot of seed solution 0.24 mL is added to the growth solution containing hexadecyltrimethyl ammonium bromide (100 mL, 0.1 M), gold (III) chloride (1.0 ml, 0.05 M), hydrochloric acid (2 mL, 1 M), ascorbic acid (0.8 ml, 0.1 M), and silver nitrate (1.2 mL, 0.01 M). The glass beaker is placed in a water
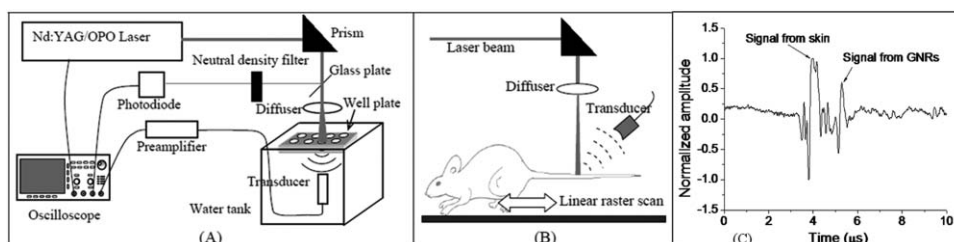

Fig. 1 (a) Schematic of the PAI setup, (b) scanning geometry on rat tail joints *in situ*, and (c) example photoacoustic signal from a rat tail joint.

bath maintained at 27°C for 3 h to complete the synthesis, and 50 mL aliquots of the synthesized rods are centrifuged at 10×10^3 rpm for 1 h to obtain pellets of GNRs at the bottom of the tube. Supernatant is decanted, and the pellet is redispersed into 5 mL of deionized water to get a concentration of 10^{13} rods/mL. The concentration of GNRs were calculated by first estimating the number of gold atoms present in a single nanorod using an average dimension of GNRs from transmission electron microscopy (TEM) images, the size of the gold atom, and the lattice spacing of the gold atom in a GNR. Then, the standard absorption of atomic gold at 400 nm was measured on a ultraviolet-visible spectrophotometry (UV-vis) instrument by preparing a standard 0.5 mM gold salt solution. Finally, the absorption of prepared GNRs solution at 400 nm is also measured. Therefore, we can calculate the amount of gold atoms in the GNR solution by the standard absorption of gold at 400 nm and, from there, estimate the concentration of GNRs. GNRs with an average aspect ratio of 4 are obtained with transverse plasmon peak at 525 nm and longitudinal plasmon peak at ~800 nm. The position of the longitudinal plasmon peak can be fine tuned fairly easily within the 600–900 nm range by varying the content of silver nitrate during synthesis.

2.5 Bioconjugation of Gold Nanorods

Bioconjugation was performed by a slightly modified method previously published by our group.[18,28–33] A layer of thiol-PEG-carboxylic acid (Laysan Bio Inc.) is reacted onto the surface of the GNRs by adding 1.0 mL of 10 mg/mL thiol-PEG-carboxylic acid solution to 1 mL of the prepared GNRs solution. The mixture is stirred for 3 h, followed by centrifugation to remove excess thiol-PEG-carboxylic acid in the solution. The layer of thiol-PEG-carboxylic acid provides the –COOH functional group required for the conjugation. The thiol-PEG-carboxylic acid-coated GNRs are dispersed in 1 mL of deionized water followed by the addition of 100 μL of 0.2 M N-ethyl-N-(3-dimethylaminopropyl) carbodiimide (EDC) and 100 μL of 0.2 M sulfo-N-hydroxy-succinimide (NHS). After waiting for 20 min, 5 μg of TNF-α antibody (R&D system) is injected to the reaction mixture. The EDC/NHS mixture forms an active ester intermediate with the GNRs, which undergoes an amidation reaction with the –NH2 group in the anti-TNF-α to yield the conjugate. The reaction mixture is stored at room temperature following centrifugation and redispersion in deionized water to remove the unconjugated antibody.

2.6 Radiolabeling of Gold Nanorods with ^{125}I

[^{125}I]Radionuclide in 10^{-5} M NaOH (pH 8–11) purchased from PerkinElmer (100 mCi/mL) was diluted with deionized water. The concentration was determined on radioactivity. GNRs (either blank or conjugated with anti-TNF-α) dispersed in fresh deionized water (0.5 mL, 10^{13} rods/mL) was added to 0.5 mL diluted [^{125}I] sodium iodide. The mixture was shaken for 30 min at room temperature. The [^{125}I]-iodine labeled GNRs were then washed with deionized water by centrifugation and redispersion.

2.7 ELISA Experiment

Two hundred microliters of 2 μg/mL human recombinant TNF-α (R&D system) in ELISA coating buffer (Immunochemistry Inc.) was added to each well of a 96-well plate and incubated for 12 h at room temperature. Then, the coating solution was aspirated out of the wells and the wells were washed twice by ELISA washing buffer (Immunochemistry Inc.). Then, 300 μL of blocking buffer was added to each well and incubated for 4 h. The blocking buffer was then aspirated out the well plates, and the plate was ready for the screening experiment. Then, 100 μL of GNRs conjugated with TNF-α antibody were added into each alternating well in row A; 100 μL GNRs conjugated with TNF-α antibody and radiolabeled (30 μCi) were added into each alternating well in row C; 100 μL radiolabeled (30 μCi) GNRs into each alternating well in row E; and 100 μL blank GNRs into each alternating well in row G. In each row, four alternating wells were used in order to average the results. After incubating the samples for 1 h, the 96-well plate was aspirated and washed with washing buffer three times. The dried plate was analyzed with PAI setup and Gamma Imager.

2.8 Rat Tail Joint Model

The GNR concentration in the original solution was 10^{13} rods/mL. The original solution was diluted 40 times, first with distilled water and then 0.2 mL of solution was mixed with 0.5 mL of I-125 with radioactivity of 400 μCi for 30 min using a ROTAMIX rotater (Appropriate Technical Resources, Inc., Laurel, Maryland). The mixture was centrifuged for 4 min at a speed of 5000 cpm in a 1-mL tube. Then, the radiolabeled GNRs at the bottom of the tube were taken out and diluted again to 0.3 mL with distilled water (~320 μCi). Therefore, in this solution (named agent 1), the GNR concentration was 10^{11} rods/mL (i.e., 2×10^{-10} M or 200 pM). After agent 1 was made, 1 mL of solution was diluted 1:1 with distilled water, which resulted in agent 2, with a GNR concentration of 1×10^{-10} M (or 100 pM). After that, 1 mL of agent 2 was diluted further 1:1 with distilled water to get agent 3, with a GNR concentration of 5×10^{-11} M (or 50 pM). As shown later in Fig. 4(a), 0.02 mL of contrast agents 1, 2, and 3 were injected intra-articularly in every other joint in the rat tail, while same amount of water (i.e., 0.02 mL each) was injected in the other two joints as control. The estimated total amount of GNRs injected in the three joints were 2×10^9, 1×10^9 and 5×10^8, respectively. Considering that some of the GNRs may stay in the upper medium in the tube after centrifuge, the actual number of GNRs injected should be slightly lower. Measured with a Capintec dose calibrator (CRC-543X, Capintec Inc., Ramsey, New Jersey), the total radioactivity of the GNRs injected into the three joints were 15.2, 7.4, and 3.6 μCi, (roughly at a ratio of 4:2:1)

This work conducted on rat tail joints is a part of our study on PAI and nuclear imaging of antirheumatic drug delivery aided by radiolabeled GNRs dual-modality contrast.[34–36] Rat tails provide good samples to study the performance of imaging on human finger or toe joints, considering their morphological similarity. Rheumatic disease rat models, including those with inflammatory arthritis, have been researched extensively and provide the opportunity to evaluate antirheumatic drugs much more quickly than in humans. In this experiment, whole tails of euthanized rats were imaged. An optical beam with size of 1 cm diam and a wavelength of 760 nm illuminated the imaged rat tail and generated photoacoustic signals that were acquired with the focused V312 Panametric transducer. The distance between
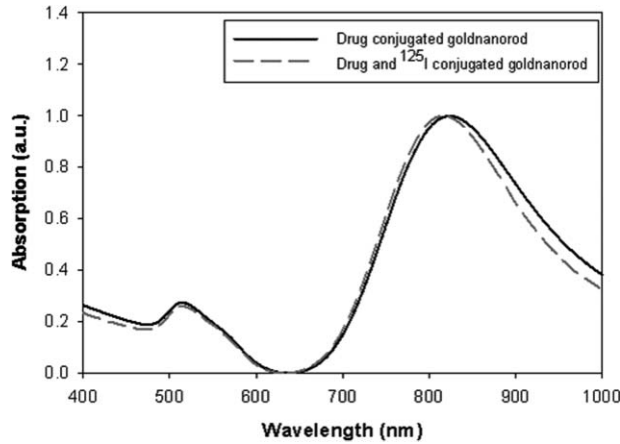
Fig. 2 UV-vis spectra of the GNRs solution before and after radiolabeling the anti-TNF-α conjugated GNRs with [125]I

the transducer and the rat tail was $\sim$19 mm, which was also the transducer focal length. Considering an f-number of 3, the estimated lateral resolution was $\sim$0.55 mm; while the estimated axial resolution was $\sim$0.12 mm. An example A-line photoacoustic signal from a rat tail joint is shown in Fig. 1(c), where the signals from the skin and the GNRs are marked. In order to acquire a 2-D image along a sagittal section of the tail, the tail immersed in water for ultrasound coupling was positioned through a computer-controlled stepper motor while the transducer and the laser beam were kept static. The scanning step was 0.6 mm (similar to the lateral resolution), and the scanning period was 60 mm (i.e., 100 steps). The total period for photoacoustic signal acquisition was $\sim$10 min when the signal at each scanning position was averaged over 50 laser pulses to achieve a better signal-to-noise ratio.

3 Results

3.1 Radiolabeling of Gold Nanorods with [125]I

The radiolabeling procedures are simple and reliable, with radiochemical yields of >80%. GNRs were found to be stable after binding with radioactive iodine. This agreed well with published data, which claim that there is high affinity and strong binding

of iodide ions to the surface of GNRs.[37] Figure 2 shows the UV-vis absorption spectra of the GNRs conjugated with TNF-α antibody before and after the addition of radioactive iodine. The minor blueshift in the spectrum is due to the change in the surrounding of the GNR's surface due to the addition of iodine molecules. The radiolabeled GNR conjugate was found to be stable for a week when stored in a refrigerator at 4°C.

3.2 ELISA Experiment

The ELISA experiment has been performed to evaluate the biological activity and the specific binding of the synthesized contrast agent carrying anti-TNF-α, which is an important therapeutic agent against arthritis. Row C with radiolabeled conjugated GNRs showed a strong signal in both the Gamma Imager and photoacoustic measurements (Fig. 3). The control in row E had a very weak photoacoustic amplitude signal and nearly zero radioactivity because the GNRs lacked the anti-TNF-α on their surface to cause specific binding on the well plate. Row A with GNRs conjugated with TNF-α antibody showed similar photoacoustic signal amplitude as row C but no radioactivity because it was not radiolabeled with [125]I. Another control of row G with blank GNRs also had a very weak photoacoustic signal and nearly zero radioactivity. The findings from the ELISA experiment conclude that the TNF-α antibody conjugated with ^{125}I labeled GNRs retains its biological activity and forms a highly specific system. The ratio of photoacoustic signal for specific (average photoacoustic amplitude from the area under row C) to nonspecific binding (average photoacoustic amplitude from the area under row E) for the targeted radiolabeled GNRs contrast agent was 6:1. The ratio of signal intensity in the γ-camera image for specific (average intensity from the area under row C) to nonspecific binding (average intensity from the area under row E) for the targeted radiolabeled GNRs contrast agent was 6.125:1. This also shows a strong one-to-one correspondence in results obtained respectively from the photoacoustic and nuclear imaging setups.

3.3 Imaging Results on Rat Tail Joints

After the first photoacoustic image was taken [Fig. 4(b)], intra-articular injections of contrast agent and water were conducted.
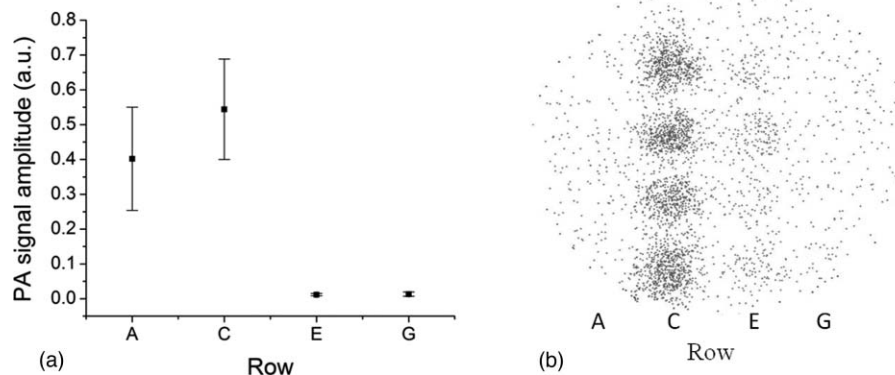
Fig. 3 (a) Mean $\pm$ standard deviation of photoacoustic signal intensity measured from each row of the ELISA plate. (b) γ-camera image of the ELISA plate. Row A contains {GNRs + anti-TNF-α}, row C contains {GNRs + anti-TNF-α + [125]I}, row E contains {GNRs + [125]I}, and row G contains {GNRs}. The photoacoustic signal and radioactive image correspond very well.
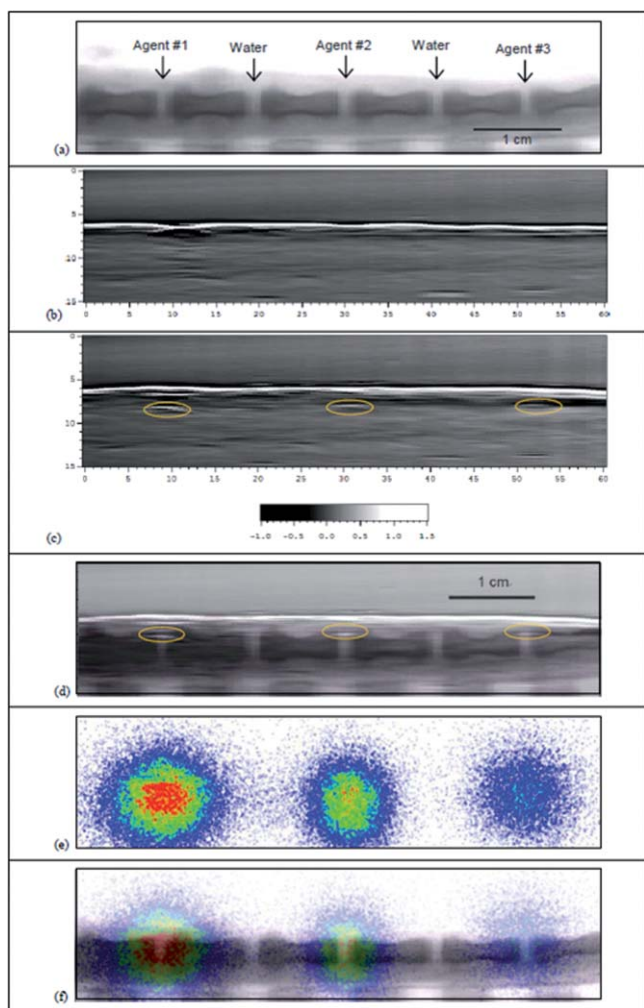
Fig. 4 *In situ* imaging of radiolabeled GNRs contrast agent in rat tail joints. (a) MicroCT image of a sagittal section of a rat tail with joint sections clearly presented. As marked in the image, intra-articular injection of contrast agent or water as control was conducted in each joint. Photoacoustic image of the sagittal section in the rat tail (b) before and (c) after intra-articular injection of contrast agent. The signal enhancements in the three joints with injected contrast agent are marked with dashed ellipses. (d) The photoacoustic image in (c) fused with the microCT image in (a). (e) SPECT image of the sagittal section in the rat tail presenting the radioactivities in the three joints with the injected contrast agent. (f) The SPECT image in (e) fused with the microCT image in (a).

Then the second photoacoustic image was taken, as shown in Fig. 4(c). The signal enhancement can be seen in the three joints with injected radiolabeled GNR contrast agent; while no noticeable change can be seen in the two joints with water injected. Because of the edge-enhancement phenomenon as a result of the limited bandwidth of the transducer,[18,38] the front contour of the volumetric contrast agent in the joint space presented the strongest signal intensity; while the photoacoustic signal from the rear contour was blocked mostly by bone. The maximum signal intensities in the three marked areas in Fig. 4(c) show a ratio of 1.16:0.60:0.27 that is close to ratio among the doses of injected contrast agent in the three joints (i.e., 4:2:1). After photoacoustic data were acquired, the rat tail was placed in our microSPECT/CT system. The 2-D images of SPECT and

CT are shown in Figs. 4(e) and 4(a), respectively. As shown in Fig. 4(a), the acquired 2-D microCT image of the sagittal section of the rat tail clearly shows the bone structure. This microCT image was then fused with the photoacoustic image in Fig. 4(c). In the microCT and photoacoustic combined image in Fig. 4(d), the photoacoustic image presents the distribution of contrast agent and some soft tissue structures; while the microCT image describes detailed bone structure in the tail. With the morphological information presented by the microCT image, we can clearly see that the positions of signal enhancements in the photoacoustic image were at the intra-articular connective tissues in the three joints containing the contrast agent.

As shown in Fig. 4(e), when the GNRs concentration in the target tissue was on the order of 10 pM, the radioactivity from ^{125}I conjugated with the GNRs was sufficient to enable nuclear imaging with an excellent signal-to-noise ratio. The counted radioactivities in the three joints with injected contrast agent were 4939, 2702, and 1453 counts/min, respectively. The ratio among them is also close to that among the contrast agent doses in the three joints (i.e., 4:2:1). In Fig. 4(f), nuclear imaging is fused with the microCT image presenting both the distribution of contrast agent and the morphological tissue structures.

4 Discussion

Notably, it is unlikely that payloads including ligands and isotopes will significantly alter the natural progression of NPs through the body with exception to designed targeting. Obviously, pharmacokinetic testing, including *in vivo* evaluation of this contrast agent, is needed to characterize how the agent in comparison to control and in pathologic settings, such as inflammatory arthritis, is treated by physiologic systems. Targeting TNF-α which are highly concentrated in inflamed tissues, NPs conjugated with anti-TNF-α could be used to quantitatively characterize the degree of inflammation within each joint affected by rheumatoid arthritis in addition to monitoring of drug delivery. This will be very helpful, particularly in animal and human studies. Limitations of the use of this contrast agent in human studies include the amount of ionization subjected to patients and, as already mentioned, potential toxicities of NPs.

Radioactive iodine-labeled compounds have been used for decades in oncology, thyroid disorder, renal function, and inflammations. By providing functional information, nuclear imaging has shown advantages in identifying the presence of abnormality where complex anatomy renders anatomic imaging (CT) less accurate. In addition, functional imaging is always necessary for pharmacokinetic study of new drugs. With the increasing proliferation of hybrid SPECT/CT recently, simultaneous acquisition of anatomic and functional information without alteration in patient position overcomes many shortcomings and results in accurate localization and metabolic characterization of the pathophysiological process. Introducing new radiopharmaceuticals and reintroducing older ones in the context of multimodality have considerably expanded. The potential benefits of combining SPECT/CT with PAI are great.

Radioactive gold NPs have typically been synthesized in the past by bombarding neutron flux on Au-197 (100% isotopic abundance) to transmute into Au-198 by neutron capture, emitting prompt γ.[39–42] The method of radiolabeling presented in this work is much simpler, green, and requires no sophisticated

equipment. Au-198 and Au-199, with strong bate emitting, provide destructive power to kill cancer cells as therapeutic agents. However, there would be a large unnecessary radiation dose to the patient if used as imaging agents. I-125 with pure γ-emitting apparently is more suitable for imaging utilization. In addition, radioactive iodine is also readily available as I-123 (γ-emitter) for SPECT, I-124 (positron emitter) for PET, and I-131 (bate emitter) for therapy. There is great potential to achieve multiple applications with a single successful compound.

With intrinsic advantages including small sizes, ease of preparation and bioconjugation, unique optical properties, as well as good biocompatibility, gold NPs (including GNRs) have been explored for potentially wide applications in drug delivery, cellular imaging, and biomedical diagnostics and therapeutics (theranostics).[43] It was shown through the ELISA experiment in this study that the anti-TNF-α molecules keep their bioactivity after conjugation to ^{125}I radiolabeled GNRs and that the conjugated system is highly specific in binding with TNF molecules. Although this work was related to imaging, delivery, and therapeutic action of anti-TNF-α, this technique of combining radiolabel functionality and other advantages of gold NPs is quite simple and stable and can easily be extended to targeted imaging and treatment of other disorders, including cancer, for instance, leukemia.[44] By introducing radiolabeled gold NPs, nuclear imaging could contribute to the understanding of how gold NPs interact with biological systems within the context of physiologically authentic environments and could accelerate the clinical applications of these agents by helping to validate and optimize their diagnostic sensitivity, cellular uptake, toxicity, and molecular response. It can also help one understand the detailed metabolic process of NPs and their accumulation in different parts of the tissues, which undoubtly has potential for many surprises.[45] We expect that radiolabeled gold NPs could also become an efficient therapy agent with the combination of the power of radiation therapy and photothermal therapy. Further work is needed to produce more efficient imaging platforms compatible with animal and human use to study the pharmacokinetics and pharmacodynamics of this contrast agent.

5 Conclusions

In this work, by imaging the ^{125}I-labeled GNRs, both PAI and SPECT have successfully resolved the distribution of GNRs conjugated to an antirheumatic agent in intra-articular connective tissues. Nuclear imaging capabilities make possible whole body imaging and in quantification due to excellent tissue transparency for γ-rays. At the same time, PAI complements these qualities with high spatial resolution on the submillimeter level (or even the micrometer level in the future when performing photoacoustic microscopy) and hence is superior in localizing contrast target in regional tissues. By fabricating the radiolabeled gold NPs conjugated with drug and performing the dual-modality imaging as described in this work, one may combine the advantage of a high contrast-to-noise ratio and simple quantification of nuclear imaging with the advantage of high spatial resolution of PAI. Using the setups described in this paper, we could image conjugated GNRs with a radioactive label of 5 μCi, down to a concentration of 10 pM in articular tissues. Imaging finding from the two modalities also correspond well with each other. This study provides evidence that the technologies of nuclear imaging and optical imaging are compatible and complementary.

References

1. I. N. Brigger, C. Dubernet, and P. Couvreur, "Nanoparticles in cancer therapy and diagnosis," *Adv. Drug Delivery Rev.* **54**(5), 631–651 (2002).
2. E. Boisselier and D. Astruc, "Gold nanoparticles in nanomedicine: preparations, imaging, diagnostics, therapies and toxicity," *Chem. Soc. Rev.* **38**(6), 1759–1782 (2009).
3. S. K. Sahoo and V. Labhasetwar, "Nanotech approaches to drug delivery and imaging," *Drug Discov. Today* **8**(24), 1112–1120 (2003).
4. M. V. Yezhelyev, X. Gao, Y. Xing, A. Al-Hajj, S. Nie, and R. M. O'Regan, "Emerging use of nanoparticles in diagnosis and treatment of breast cancer," *Lancet Oncol.* **7**(8), 657–667 (2006).
5. A. M. Morawski, P. M. Winter, K. C. Crowder, S. D. Caruthers, R. W. Fuhrhop, M. J. Scott, J. D. Robertson, D. R. Abendschein, G. M. Lanza, and S. A. Wickline, "Targeted nanoparticles for quantitative imaging of sparse molecular epitopes with MRI," *Magn. Reson. Med.* **51**(3), 480–486 (2004).
6. X. Wang, Y. Pang, G. Ku, X. Xie, G. Stoica, and L. V. Wang, "Noninvasive laser-induced photoacoustic tomography for structural and functional *in vivo* imaging of the brain," *Nat. Biotechnol.* **21**(7), 803–806 (2003).
7. X. Wang, Y. Pang, G. Ku, G. Stoica, and L. V. Wang, "Three-dimensional laser-induced photoacoustic tomography of mouse brain with the skin and skull intact," *Opt. Lett.* **28**(19), 1739–1741 (2003).
8. C. G. A. Hoelen, F. F. M. De Mul, R. Pongers, and A. Dekker, "Three-dimensional photoacoustic imaging of blood vessels in tissue," *Opt. Lett.* **23**(8), 648–650 (1998).
9. M. Xu and L. V. Wang, "Photoacoustic imaging in biomedicine," *Rev. Sci. Instrum.* **77**, 041101 (2006).
10. X. Wang, G. Ku, M. A. Wegiel, D. J. Bornhop, G. Stoica, and L. V. Wang, "Noninvasive photoacoustic angiography of animal brains *in vivo* with near-infraredlight and an optical contrast agent," *Opt. Lett.* **29**(7), 730–732 (2004).
11. J. A. Copland, M. Eghtedari, V. L. Popov, N. Kotov, N. Mamedova, M. Motamedi, and A. A. Oraevsky, "Bioconjugated gold nanoparticles as a molecular based contrast agent: implications for imaging of deep tumors using optoacoustic tomography," *Mol. Imaging Biol.* **6**(5), 341–349 (2004).
12. K. H. Song, E. W. Stein, J. A. Margenthaler, and L. V. Wang, "Noninvasive photoacoustic identification of sentinel lymph nodes containing methylene blue *in vivo* in a rat model," *J. Biomed. Opt.* **13**(5), 054033 (2008).
13. C. H. Li and L. H. V. Wang, "Photoacoustic tomography and sensing in biomedicine," *Phys. Med. Biol.* **54**(19), R59–R97 (2009).
14. X. Yang, S. E. Skrabalak, Z.-Y. Li, Y. Xia, and L. V. Wang, "Photoacoustic tomography of a rat cerebral cortex *in vivo* with Au nanocages as an optical contrast agent," *Nano Lett.* **7**(12), 3798–3802 (2007).
15. Y. Wang, X. Xie, X. Wang, G. Ku, K. L. Gill, D. P. O'Neal, G. Stoica, and L. V. Wang, "Photoacoustic tomography of a nanoshell contrast agent in the *in vivo* rat brain," *Nano Lett.* **4**(9), 1689–1692 (2004).
16. A. Agarwal, S. W. Huang, M. O'Donnell, K. C. Day, M. Day, N. Kotov, and S. Ashkenazi, "Targeted gold nanorod contrast agent for prostate cancer detection by photoacoustic imaging," *J. Appl. Phys.* **102**(6), 064701 (2007).
17. K. Kim, S. W. Huang, S. Ashkenazi, M. O'Donnell, A. Agarwal, N. A. Kotov, M. F. Denny, and M. J. Kaplan, "Photoacoustic imaging of early inflammatory response using gold nanorods," *Appl. Phys. Lett.* **90**(22), 223901 (2007).
18. D. L. Chamberland, A. Agarwal, N. Kotov, J. Brian Fowlkes, P. L. Carson, and X. Wang, "Photoacoustic tomography of joints aided by an Etanercept-conjugated gold nanoparticle contrast agent—an *ex vivo* preliminary rat study," *Nanotechnology* **19**, 095101 (2008).

19. G. Han, P. Ghosh, M. De, and V. Rotello, "Drug and gene delivery using gold nanoparticles," *NanoBioTechnol.* **3**(1), 40–45 (2007).

20. X. Huang, P. Jain, I. El-Sayed, and M. El-Sayed, "Plasmonic photothermal therapy (PPTT) using gold nanoparticles," *Lasers Med. Sci.* **23**(3), 217–228 (2008).

21. G. von Maltzahn, J.-H. Park, A. Agrawal, N. K. Bandaru, S. K. Das, M. J. Sailor, and S. N. Bhatia, "Computationally guided photothermal tumor therapy using long-circulating gold nanorod antennas," *Cancer Res.* **69**(9), 3892–3900 (2009).

22. M. C. Pierce, D. J. Javier, and R. Richards-Kortum, "Optical contrast agents and imaging systems for detection and diagnosis of cancer," *Int. J. Cancer* **123**(9), 1979–1990 (2008).

23. S. R. Cherry, "*In vivo* molecular and genomic imaging: new challenges for imaging physics," *Phys. Med. Biol.* **49**(3), 13–49 (2004).

24. E. Carbo-Argibay, B. Rodriguez-Gonzalez, J. Pacifico, I. Pastoriza-Santos, J. Perez-Juste, and L. M. Liz-Marzan, "Chemical sharpening of gold nanorods: the rod-to-octahedron transition," *Angew Chem. Int. Edit.* **46**(47), 8983–8987 (2007).

25. L. Gou and C. J. Murphy, "Fine-tuning the shape of gold nanorods," *Chem. Mater.* **17**(14), 3668–3672 (2005).

26. B. Nikoobakht and M. A. El-Sayed, "Preparation and growth mechanism of gold nanorods (NRs) using seed-mediated growth method," *Chem. Mater.* **15**(10), 1957–1962 (2003).

27. J. Perez-Juste, I. Pastoriza-Santos, L. M. Liz-Marzan, and P. Mulvaney, "Gold nanorods: synthesis, characterization and applications," *Coord. Chem. Rev.* **249**(17–18), 1870–1901 (2005).

28. R. Popovtzer, A. Agrawal, N. A. Kotov, A. Popovtzer, J. Balter, T. E. Carey, and R. Kopelman, "Targeted gold nanoparticles enable molecular CT imaging of cancer," *Nano Lett.* **8**(12), 4593–4596 (2008).

29. K. Kim, S. W. Huang, S. Ashkenazi, M. O'Donnell, A. Agarwal, N. A. Kotov, M. F. Denny, and M. J. Kaplan, "Photoacoustic imaging of early inflammatory response using gold nanorods," *Appl. Phys. Lett.* **90**, 223901 (2007).

30. A. Agarwal, S. W. Huang, M. O'Donnell, K. C. Day, M. Day, N. Kotov, and S. Ashkenazi, "Targeted gold nanorod contrast agent for prostate cancer detection by photoacoustic imaging," *J. Appl. Phys.* **102**, 064701 (2007).

31. J. Lee, A. O. Govorov, J. Dulka, and N. A. Kotov, "Bioconjugates of CdTe nanowires and Au nanoparticles: plasmon- exciton interactions, luminescence enhancement, and collective effects," *Nano Lett.* **4**(12), 2323–2330 (2004).

32. S. Wang, N. Mamedova, N. A. Kotov, W. Chen, and J. Studer, "Antigen/antibody immunocomplex from CdTe nanoparticle bioconjugates," *Nano Lett.* **2**(8), 817–822 (2002).

33. N. N. Mamedova, N. A. Kotov, A. L. Rogach, and J. Studer, "Albumin-CdTe nanoparticle bioconjugates: preparation, structure, and interunit energy transfer with antenna effect," *Nano Lett.* **1**(6), 281–286 (2001).

34. D. L. Chamberland, J. D. Taurog, J. A. Richardson, and X. Wang, "Photoacoustic tomography: a new imaging technology for inflammatory arthritis—as applied to tail spondylitis in rats," *Clin. Exp. Rheumatol.* **27**(2), 387–388 (2009).

35. D. L. Chamberland, X. Wang, and B. J. Roessler, "Photoacoustic tomography of carrageenan-induced arthritis in a rat model," *J. Biomed. Opt.* **13**(1), 011005 (2008).

36. X. Wang, D. L. Chamberland, P. L. Carson, J. B. Fowlkes, R. O. Bude, D. A. Jamadar, and B. J. Roessler, "Imaging of joints with laser-based photoacoustic tomography: an animal study," *Med. Phys.* **33**(8), 2691–2697 (2006).

37. M. Grzelczak, A. Sanchez-Iglesias, B. Rodriguez-Gonzalez, R. Alvarez-Puebla, J. Perez-Juste, and L. M. Liz-Marzan, "Influence of iodide ions on the growth of gold nanorods: tuning tip curvature and surface plasmon resonance," *Adv. Funct. Mater.* **18**(23), 3780–3786 (2008).

38. L. S. Bouchard, M. S. Anwar, G. L. Liu, B. Hann, Z. H. Xie, J. W. Gray, X. Wang, A. Pines, and F. F. Chen, "Picomolar sensitivity MRI and photoacoustic imaging of cobalt nanoparticles," *Proc. Natl. Acad. Sci. USA* **106**(11), 4085–4089 (2009).

39. K. V. Katti, R. Kannan, K. Katti, V. Kattumori, R. Pandrapraganda, V. Rahing, C. Cutler, E. J. Boote, S. W. Casteel, C. J. Smith, J. D. Robertson, and S. S. Jurrison, "Hybrid gold nanoparticles in molecular imaging and radiotherapy," *Czech. J. Phys.* **56**(1), D23–D34 (2006).

40. K. Roy and S. Lahiri, "A green method for synthesis of radioactive gold nanoparticles," *Green Chem.* **8**(12), 1063–1066 (2006).

41. R. Kannan, V. Rahing, C. Cutler, R. Pandrapragada, K. K. Katti, V. Kattumuri, J. D. Robertson, S. J. Casteel, S. Jurisson, and C. Smith, "Nanocompatible chemistry toward fabrication of target-specific gold nanoparticles," *J. Am. Chem. Soc.* **128**(35), 11342–11343 (2006).

42. N. Chanda, P. Kan, L. D. Watkinson, R. Shukla, A. Zambre, T. L. Carmack, H. Engelbrecht, J. R. Lever, K. Katti, G. M. Fent, S. W. Casteel, C. J. Smith, W. H. Miller, S. Jurisson, E. Boote, J. D. Robertson, C. Cutler, M. Dobrovolskaia, R. Kannan, and K. V. Katti, "Radioactive gold nanoparticles in cancer therapy: therapeutic efficacy studies of GA-198AuNP nanoconstruct in prostate tumor–bearing mice," *Nanomedicine* **6**(2), 201–209 (2010).

43. W. Chen, N. F. Xu, L. G. Xu, L. B. Wang, Z. K. Li, W. Ma, Y. Y. Zhu, C. L. Xu, and N. A. Kotov, "Multifunctional magnetoplasmonic nanoparticle assemblies for cancer therapy and diagnostics (theranostics)," *Macromol. Rapid Comm.* **31**(2), 228–236 (2010).

44. P. Podsiadlo, V. A. Sinani, J. H. Bahng, N. W. Kam, J. Lee and N. A. Kotov, "Gold nanoparticles enhance the anti-leukemia action of a 6-mercaptopurine chemotherapeutic agent," *Langmuir* **24**(2), 568–574 (2008).

45. N. A. Kotov, "Chemistry: inorganic nanoparticles as protein mimics," *Science* **330**(6001), 188–189 (2010).